Coarse-grained non-equilibrium simulations of crystalline materials at nano scale

X Wang and **J D Lee***
Department of Mechanical and Aerospace Engineering, George Washington University, Washington, DC 20052, USA

The manuscript was received on 29 October 2010 and was accepted after revision for publication on 7 February 2011.

DOI: 10.1177/1740349911402137

Abstract: This paper presents a coarse-grained non-equilibrium simulation (CG-NES) model based on an atom-based continuum (ABC) method for the multi-element crystal. The main objective of CG-NES model is to establish a nodal ensemble that provides a more efficient way to compute the thermal properties for non-equilibrium systems. In this work, a generalized Nosé-Hoover thermostat network is proposed for each finite element node to control the temperature of the system. Several numerical examples have been carried out and it has been demonstrated that CG-NES has the capability and efficiency to study the non-equilibrium system, including thermal-mechanical coupling phenomena and thermal-electromagnetic effects.

Keywords: molecular dynamics, finite element method, non-equilibrium, nanomechanics, coarse-grained simulation, Nosé-Hoover thermostat

1 INTRODUCTION

Nanomaterials reveal many excellent mechanical, thermal, and electronic properties. In particular, the thermal properties are of great interest because of their strong relevance to the potential application in nanoscale thermoelectric energy generators or on-chip coolers. The non-equilibrium thermal-mechanical process at small scales, for instance nanoscale heat transfer, in which the length and/or time scales span from the molecular to the continuum, is a subject of increasing importance to energy conversion, biotechnology, microelectronics, biochemical detection, and material synthesis and failure analysis. The capacity to simulate thermal-mechanical couplings in non-equilibrium states at small scales is vital to the understanding of transport mechanisms of energy conversion and to the advancement of reliability of micro and nano-electronics.

Since the thermal behaviour of nanostructured materials or nanoelectronic devices cannot be simply inferred by extrapolating macroscopic behaviour to small scales, many experimental studies have been performed to measure these thermal characteristics [**1–4**]. However, the best experimental resolution is still larger than 100 nm. Non-equilibrium molecular dynamics (NEMD) has become a major tool to simulate thermo-mechanical processes. It has been extensively used in engineering and applied physics communities, and it has become the workhorse in performing direct atomistic or molecular simulations in nanoscale heat transfer [**5–10**], polymer and amorphous materials [**11–14**], gas transport in nanopores [**15**], and so on.

In recent years, several multiscale methods have been proposed to solve nanoscale thermo-mechanical problems, and they have been successful for certain problems, for example, Abraham and co-workers' macroscopic, atomistic, *ab initio* dynamics (MAAD) [**16**], Rudd and Broughton's coarse-grained molecular dynamics (CGMD) [**17**], Liu and co-workers' bridging scale method [**18**, **19**], E and his co-workers' heterogeneous multiscale method [**20–22**], and Li and his co-workers' multiscale non-equilibrium molecular dynamics (MS-NEMD) [**23–25**], and so on.

In this paper, a coarse-grained non-equilibrium simulation (CG-NES) model is proposed based on

**Corresponding author: Department of Mechanical and Aerospace Engineering, George Washington University, Washington, DC 20052, USA*
email: jdlee@gwu.edu

an the atom-based continuum (ABC) method for multi-element crystals. To enhance the computational efficiency, a cluster-based force calculation rule is used in the finite element (FE) formulation and a distributed Nosé-Hoover thermostat network is employed for each FE node to control the temperature of the system. The organization of the remainder of the paper is as follows: Section 2 briefly presents the Nosé-Hoover thermostat and NEMD simulation. In section 3 the atom-based continuum method is introduced. Then the coarse-grained non-equilibrium method and its numerical results are presented in sections 4 and 5, respectively. Finally, a brief summary and discussion are given in section 6.

2 NOSÉ-HOOVER THERMOSTAT AND NON-EQUILIBRIUM MOLECULAR DYNAMICS SIMULATION

Classical molecular dynamics simulations are performed in the microcanonical ensemble, meaning that the volume, the number of atoms, and the energy are controlled. It is not possible to provide statistical characters to the physical problem that it simulates. To extrapolate statistical thermodynamics information from molecular dynamics simulations, the performance of equilibrium ensemble molecular dynamics are required at a fixed temperature or fixed pressure or specified chemical potentials. Several methods have been introduced to keep the temperature constant while using the microcanonical ensemble. Popular techniques to control temperature include velocity rescaling [**26–32**], the Nosé-Hoover thermostat [**33**, **34**], Nosé-Hoover chains [**35**], and the Berendsen thermostat [**36**]. The central idea is to simulate in such a way that a canonical distribution is obtained. Here the essence of Nosé-Hoover equilibrium MD is briefly introduced, which is the most popular scheme within the molecular dynamics community.

In order to maintain a fixed temperature for a whole system shown in Fig. 1(a) (for the purpose of illustration, the figure is plotted as if in two dimensions), the atomistic or molecular system is regularized by a Nosé-Hoover thermostat. The governing equation of Nosé-Hoover MD simulation takes the following form

$$m^i\ddot{\boldsymbol{x}}^i(t)=\boldsymbol{f}^i(t)-m^i\chi(t)\dot{\boldsymbol{x}}^i(t) \tag{1}$$

where $\boldsymbol{x}^i(t)$ is the position of the ith atom; m^i is its mass; $\boldsymbol{f}^i(t)$ is the interatomic force acting on the ith atom; $\dot{\boldsymbol{x}}^i(t)=d\boldsymbol{x}^i(t)/dt$; $\ddot{\boldsymbol{x}}^i(t)=d^2\boldsymbol{x}^i(t)/dt^2$; and $\chi(t)$ is a friction coefficient that may be controlled by the following equation

$$\frac{d\chi(t)}{dt}=\frac{1}{Q}\left\{\sum_{j=1}^{N}m^j\left[\dot{\boldsymbol{x}}^j(t)\right]^2-3Nk_BT_{\text{eqb}}\right\} \tag{2}$$

where N is the total number of atoms in the whole system; T_{eqb} is the equilibrium or expected temperature; $Q=3Nk_BT_{\text{eqb}}\tau_T^2$ is the effective 'mass' of the thermostat, τ_T is a specified time constant (normally in the range [0.5, 2] ps). Consequently, temperature can be calculated as a space-averaged variable

$$3Nk_BT=\sum_{i=1}^{N}m^i(\boldsymbol{v}^i)^2 \tag{3}$$

where $\boldsymbol{v}^i=\dot{\boldsymbol{x}}^i$.

The action of the thermostat can be understood in the following terms. Whenever the (kinetic) temperature of the atoms in the whole system T is larger than T_{eqb}, $\chi(t)$ increases and eventually becomes positive. Accordingly, the friction acts as a dissipation agent which will reduce the temperature (cf. equation (1)). Since the opposite occurs whenever the temperature falls below T_{eqb}, the Nosé-Hoover thermostat represented by $-m^i\chi(t)\dot{\boldsymbol{x}}^i(t)$ acts as a stabilizing feedback around the prescribed temperature.

However, for non-equilibrium systems, the equilibrium MD becomes incapable of simulating problems with spatial temperature gradients. Motivated by how to overcome the difficulties of dealing with the stochastic process, since the early 1980s the NEMD has become a major simulation tool for non-equilibrium processes, especially in computing transport coefficients and simulating viscous flows. For the direct NEMD simulation depicted in Fig. 1(b), only the boundary regions Ω_+ and Ω_- are controlled with the temperature $T_{\text{eqb}+}$ and $T_{\text{eqb}-}$, respectively. We denote $V_\pm$ as the two sets of N_+ atoms in Ω_+ in contact with the reservoirs. The evolution of the atoms in the thermal contact with the reservoirs is ruled by the equation

$$m^i\ddot{\mathbf{x}}^i(t)=\mathbf{f}^i(t)-\begin{cases}m^i\chi_+(t)[\mathbf{v}^i(t)-\mathbf{v}_+(t)+\Delta\mathbf{v}_+^i(t)] & \text{if } i\in V_+\\ m^i\chi_-(t)[\mathbf{v}^i(t)-\mathbf{v}_-(t)+\Delta\mathbf{v}_-^i(t)] & \text{if } i\in V_-\end{cases} \tag{4}$$

where $\chi_\pm$ are the two friction coefficients modelling the microscopic action of the thermostat; $\Delta\boldsymbol{v}_\pm^i(t)$ is called the thermostat's auxiliary velocity to make sure that the linear and angular momenta of the two thermostats are unchanged during the whole

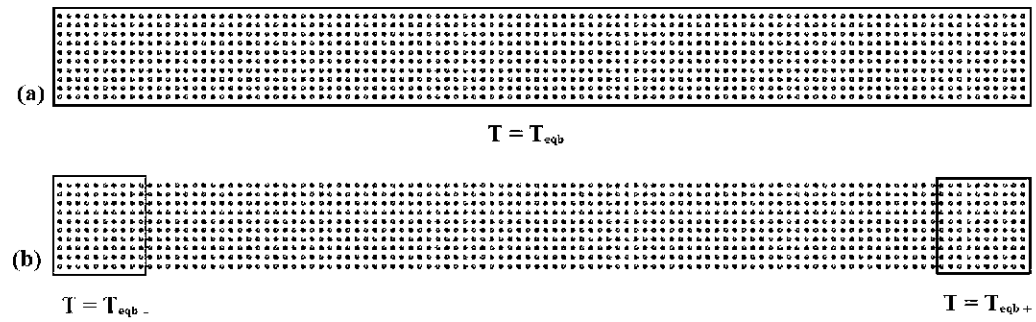

Fig. 1 Molecular dynamics with finite temperature: (a) the Nosé-Hoover equilibrium MD simulation; (b) the direct NEMD simulation

process (see Appendix). The dynamics of χ_+ is governed by the equation

$$\frac{d\chi_{\pm}(t)}{dt} = \frac{1}{Q_{\pm}}\left\{\sum_{j=1}^{N_{\pm}} m^j\left[\dot{\boldsymbol{x}}^j(t) - \boldsymbol{v}_{\pm}(t)\right]^2 - 3k_B N_{\pm} T_{\mathrm{eqb}\pm}\right\} \tag{5}$$

where $\boldsymbol{v}_{\pm}(t)$ is the average velocity of $\Omega_{\pm}$. It can be noticed that equations (4) and (5) will not be reduced to equations (1) and (2) even if $T_{\mathrm{eqb}+} = T_{\mathrm{eqb}-} = T_{\mathrm{eqb}}$ is chosen. The reason is that in the direct NEMD simulation, the interior domain is not controlled.

To improve the computational efficiency and to broaden the applications of NEMD, it is necessary to develop a coarse-grained non-equilibrium simulation (CG-NES) technique with direct simulations of non-equilibrium systems with spatial temperature gradients.

In the proposed CG-NES, a vital step is the use of the peculiar and the associated centre of mass (COM) coordinates, with which it is possible to rigorously extract thermodynamics properties of the system from the drifting frame of reference. For a finite thermodynamic system which undergoes large deformation, it may be insufficient to use only one set of COM coordinates. To solve this non-equilibrium system more accurately, a set of local peculiar and COM coordinates are defined to obtain the local peculiar velocities [**23**–**25**]. Through the atom-based continuum method described later, the concepts of the peculiar and COM coordinates are generalized to establish the FE nodes corresponding to the generalized COM coordinate and the unit cells within the finite elements corresponding to the generalized peculiar coordinates. Hence, the atom-based continuum is the foundation of the CG-NES algorithm.

3 AN ATOM-BASED CONTINUUM (ABC) METHOD

3.1 Lattice dynamics

Note that a multi-element crystalline material (which has more than one kind of atom in the unit cell) is distinguished from other states of matter by a periodic arrangement of the atoms, which can be represented as a collection of lattice cells and a group of discrete and distinct atoms situated within each lattice cell as depicted in Fig. 2. Consider a system consisting of N_1 lattice cells; each lattice cell k is composed of N_a atoms with mass m^α [$\alpha = 1, 2, 3, \ldots, N_a$], positions in the reference configuration $\boldsymbol{X}^{k\alpha}$, positions in the current configuration $\boldsymbol{x}^{k\alpha}(t)$, displacements $\boldsymbol{u}^{k\alpha}(t) = \boldsymbol{x}^{k\alpha}(t) - \boldsymbol{X}^{k\alpha}$, and velocities $\dot{\boldsymbol{u}}^{k\alpha}(t)$. Herein, the superscript $k\alpha$ refers to the αth atom in the kth lattice cell; and $\dot{\boldsymbol{u}}^{k\alpha} \equiv d\boldsymbol{u}^{k\alpha}/dt$.

The initial configuration of each lattice cell in a single crystalline material can be identified by its lattice coordinates $\boldsymbol{l} = (l_1, l_2, l_3)$, where l_i are integers. So the spatial initial position $\boldsymbol{X}^k$ of the kth lattice cell is defined as

$$\boldsymbol{X}^k = \sum_{a=1}^{3} l_a \boldsymbol{B}_a \tag{6}$$

where $\boldsymbol{B}_a$ are the basis vectors spanning a simple three-dimensional (3D) Bravais lattice.

It is assumed that the total potential energy V of the system mentioned above can be additively computed as the sum of energies of each atom

$$V = \sum_k \sum_\alpha V^{k\alpha} \tag{7}$$

where $V^{k\alpha}$ is the sum of the energies owing to any interatomic potential, such as pair-wise interaction

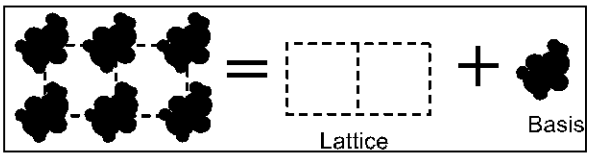

Fig. 2 Atomistic view of crystal structure

of the atoms, three-body potentials, or other many-body potentials, including the Tersoff and the Stillinger-Weber potentials. $V^{k\alpha}$ can be expressed in a general form

$$V^{k\alpha}=\frac{1}{2!}\sum_{l}\sum_{\beta}V_2(\boldsymbol{x}^{k\alpha},\boldsymbol{x}^{l\beta})+\frac{1}{3!}\sum_{l,m}\sum_{\beta,\gamma}V_3(\boldsymbol{x}^{k\alpha},\boldsymbol{x}^{l\beta},\boldsymbol{x}^{m\gamma})+\cdots \tag{8}$$

with the understanding $(k,\alpha)\neq(l,\beta)\neq(m,\gamma)\neq\ldots$.

The particular form of the interatomic potential energy depends on the model of atomic interactions. In this work, the pair potential is employed and the potential energy of the atom $k\alpha$ is

$$V^{k\alpha}=\frac{1}{2}\sum_{l}\sum_{\beta}V_2(\boldsymbol{x}^{k\alpha},\boldsymbol{x}^{l\beta})\equiv\frac{1}{2}\sum_{l}\sum_{\beta}V^{k\alpha\ \ l\beta}(\boldsymbol{x}^{k\alpha},\boldsymbol{x}^{l\beta}) \tag{9}$$

The governing equation of any atom $k\alpha$ in the system can be expressed as

$$m^{\alpha}\ddot{\boldsymbol{u}}^{k\alpha}=\boldsymbol{f}^{k\alpha}+\boldsymbol{\varphi}^{k\alpha} \tag{10}$$

where $\dot{\boldsymbol{u}}^{k\alpha}=\dot{\boldsymbol{x}}^{k\alpha}$; $\ddot{\boldsymbol{u}}^{k\alpha}=\ddot{\boldsymbol{x}}^{k\alpha}$; $\boldsymbol{f}^{k\alpha}=\sum_l\sum_\beta\boldsymbol{f}^{k\alpha\ \ l\beta}$; $\boldsymbol{\varphi}^{k\alpha}$ is the external force acting on the $k\alpha$ atom including damping force; $\boldsymbol{f}^{k\alpha-l\beta}$ is the atomic force acting on the $k\alpha$ atom owing to the $l\beta$ atom, which is the negative derivative of the potential energy $V^{k\alpha-l\beta}(\boldsymbol{x}^{k\alpha},\boldsymbol{x}^{l\beta})$ with respect to the atom's current position vector $\boldsymbol{x}^{k\alpha}$

$$\boldsymbol{f}^{k\alpha-l\beta}=-\frac{\partial V^{k\alpha-l\beta}(d^{k\alpha-l\beta})}{\partial d^{k\alpha\ \ l\beta}} \tag{11}$$

and here it is also assumed that the potential energies depend only on the relative interatomic distance $d^{k\alpha-l\beta}\equiv\|\boldsymbol{x}^{k\alpha}-\boldsymbol{x}^{l\beta}\|$, so

$$\boldsymbol{f}^{k\alpha\ \ l\beta}=-\frac{\partial V^{k\alpha-l\beta}(d^{k\alpha-l\beta})}{\partial d^{k\alpha-l\beta}}\frac{\partial d^{k\alpha-l\beta}}{\partial \boldsymbol{x}^{k\alpha}}=-\frac{\partial V^{k\alpha-l\beta}(d^{k\alpha-l\beta})}{\partial d^{k\alpha\ \ l\beta}}\frac{\boldsymbol{x}^{k\alpha}-\boldsymbol{x}^{l\beta}}{d^{k\alpha\ \ l\beta}}=-\boldsymbol{f}^{l\beta-k\alpha} \tag{12}$$

3.2 Kinematic constrains

For the purpose of large-scale simulation of collaborative material behaviour, an approximation solution to equation (10) is desired. Therefore, the reduction of degrees of freedom is accomplished by virtue of kinematic constrains, i.e. through the shape functions in the FE method. Some judiciously selected lattice cells, called FE nodes, retain their independent degrees of freedom. Z is the set of all lattice cells; Z_N is the set of all FE nodes; $Z_N\subseteq Z$. The nodal displacements together with shape functions are employed to determine a displacement field, in other words, all other lattice cells are forced to follow the motion of the nodes – this is what is referred to as 'kinematic constraint', which is the practice in every FE analysis. The density of FE nodes is controlled by a criterion that measures how strong the deformation varies spatially. The displacement $\boldsymbol{u}^{k\alpha}$ is approximated by FE interpolation from its nodal values $\mathbf{U}_I^{\alpha}$ as

$$\boldsymbol{u}^{k\alpha}=\sum_{I}\Phi_I(k)\mathbf{U}_I^{\alpha} \tag{13}$$

where $\Phi_I(k)$ is Ith shape function of the kth lattice cell; $\mathbf{U}_I^{\alpha}$ is the displacements of the α atom of the Ith node of the element in which the kth lattice cell resides.

Following the standard procedure of Galerkin method, the weak form of equation (10) is written as follows

$$\sum_k\sum_\alpha m^{\alpha}\ddot{\boldsymbol{u}}^{k\alpha}\delta\boldsymbol{u}^{k\alpha}=\sum_k\sum_\alpha\sum_l\sum_\beta\boldsymbol{f}^{k\alpha-l\beta}\delta\boldsymbol{u}^{k\alpha}+\sum_k\sum_\alpha\boldsymbol{\varphi}^{k\alpha}\delta\boldsymbol{u}^{k\alpha} \tag{14}$$

In light of $\boldsymbol{f}^{k\alpha-l\beta}=-\boldsymbol{f}^{l\beta-k\alpha}$, equation (14) is rewritten as

$$\sum_k\sum_\alpha m^{\alpha}\ddot{\boldsymbol{u}}^{k\alpha}\delta\boldsymbol{u}^{k\alpha}=\frac{1}{2}\sum_k\sum_\alpha\sum_l\sum_\beta\{\boldsymbol{f}^{k\alpha-l\beta}-\boldsymbol{f}^{l\beta-k\alpha}\}\delta\boldsymbol{u}^{k\alpha}+\sum_k\sum_\alpha\boldsymbol{\varphi}^{k\alpha}\delta\boldsymbol{u}^{k\alpha} \tag{15}$$

which can also be written as

$$\sum_k\sum_\alpha m^{\alpha}\ddot{\boldsymbol{u}}^{k\alpha}\delta\boldsymbol{u}^{k\alpha}=\frac{1}{2}\sum_k\sum_\alpha\sum_l\sum_\beta\boldsymbol{f}^{k\alpha\ \ l\beta}\{\delta\boldsymbol{u}^{k\alpha}-\delta\boldsymbol{u}^{l\beta}\}+\sum_k\sum_\alpha\boldsymbol{\varphi}^{k\alpha}\delta\boldsymbol{u}^{k\alpha} \tag{16}$$

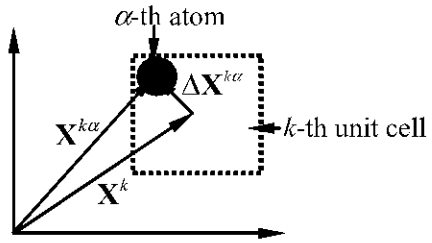

Fig. 3 Position descriptions in the reference configuration

By virtue of $\delta \boldsymbol{u}^{k\alpha} = \sum_I \Phi_I(k) \delta \mathbf{U}_I^\alpha$, the governing equations for nodal displacements $\mathbf{U}_I^\alpha$ can be expressed as

$$\left(\sum_J M_{IJ}^\alpha \right) \ddot{\mathbf{U}}_J^\alpha = \mathbf{F}_I^\alpha + \mathbf{\Phi}_I^\alpha \tag{17}$$

where

$$M_{IJ}^\alpha = \sum_k m^\alpha \Phi_J(k) \Phi_I(k) = M_{JI}^\alpha \tag{18}$$

$$\begin{aligned} \mathbf{F}_I^\alpha = & \frac{1}{2} \sum_k \sum_l \sum_\beta \boldsymbol{f}^{k\alpha - l\beta} \Phi_I(k) \\ & - \frac{1}{2} \sum_k \sum_l \sum_\gamma \boldsymbol{f}^{k\gamma \ \ l\alpha} \Phi_I(l) \end{aligned} \tag{19}$$

$$\mathbf{\Phi}_I^\alpha = \sum_k \varphi^{k\alpha} \mathbf{\Phi}_I(k) \tag{20}$$

The existence of superscript α in equation (17) implies that the atomic information is naturally built in the ABC method and the internal relaxation is allowed in each node to represent an atomistic multi-element system. It is also noticed that, in equations (19) and (20), full-blown non-locality, non-linearity, and atom-based constitutive relations are automatically rooted in the force calculation. So a fully non-local ABC formulation has been proposed.

In practice, the consistent mass matrix is commonly replaced by a lumped matrix for computational convenience. Here the 'row-sum' lumping technique is utilized, and then equation (17) can be rewritten as

$$\tilde{M}_I^\alpha \ddot{\mathbf{U}}_I^\alpha = \mathbf{F}_I^\alpha + \mathbf{\Phi}_I^\alpha \tag{21}$$

3.3 Summation rule for force calculation

All summations in equations (18) to (20) are normally carried out by numerical quadrature. In Fig. 4, it is seen that around each node (an open circle), say the Jth node, there is a cluster (a shaded area), named ψ_J. From now on, force calculation is no longer performed for all unit cells in the entire system, but for all clusters. A representative unit cell (a black solid square) is the unit cell within one of $\psi_J = \{l : |\mathbf{X}_l - \mathbf{X}_J| \leqslant R_J\}$. Notice that there is no overlapping of clusters. $\boldsymbol{X}_l$ is the position of the lth unit cell and R_J is the radius of the cluster ψ_J centred at the Jth node. The cluster summation rule for equation (19) reads

$$\begin{aligned} \mathbf{F}_J^\alpha = & \frac{1}{2} \sum_k \sum_l \sum_\beta \boldsymbol{f}^{k\alpha \ \ l\beta} \Phi_J(k) \\ & - \frac{1}{2} \sum_k \sum_l \sum_\gamma \boldsymbol{f}^{k\gamma - l\alpha} \Phi_J(l) \\ = & \frac{1}{2} \sum_{I \in \mathbb{Z}_N} w_I \sum_{j \in \psi_I} \sum_{l=1}^{N_l} \sum_{\beta=1}^{N_a} \boldsymbol{f}^{j\alpha \ \ l\beta} \Phi_J(j) \\ & - \frac{1}{2} \sum_{I \in \mathbb{Z}_N} w_I \sum_{j \in \psi_I} \sum_{l=1}^{N_l} \sum_{\gamma=1}^{N_a} \boldsymbol{f}^{j\gamma - l\alpha} \Phi_J(l) \end{aligned} \tag{22}$$

where $w_I (I \in Z_N)$, the weight of the Ith cluster. When the size of clusters shrink to nodes, i.e. $\psi_J = \{J\} \ \ \forall J \in Z_N$, it holds $\Phi_I(J) = \delta_{IJ}$, and the cluster summation rule boils down to a node-based summation rule

$$\begin{aligned} \mathbf{F}_J^\alpha = & \frac{1}{2} \sum_{I \in \mathbb{Z}_N} w_I \sum_{l=1}^{N_l} \sum_{\beta=1}^{N_a} \delta_{JI} \boldsymbol{f}^{I\alpha - l\beta} \\ & - \frac{1}{2} \sum_{I \in \mathbb{Z}_N} w_I \sum_{l=1}^{N_l} \sum_{\gamma=1}^{N_a} \boldsymbol{f}^{I\gamma - l\alpha} \Phi_J(l) \end{aligned} \tag{23}$$

In this case the weighting factor w_I is the number of unit cells represented by Ith node, thus. At the other extreme, $w_I = \sum_{j=1}^{N_l} \Phi_I(j) \ \ \forall I \in Z_N$. At the other extreme, $w_I = 1 \forall I \in Z_N$ implies that all pairs of interatomic forces are calculated. In all cases $\sum_{I \in Z_N} \sum_{j \in \psi_I} n_j = N_l$ holds.

Figure 4 shows the numerical procedures to calculate the interatomic force between any two atoms. The force between any two atoms in the atomic region is treated exactly the same way as in MD simulation. In the continuum region the force between any two atoms in different or the same unit cells should be distributed to all the nodes of the elements, in which the two unit cells reside. For example, there is a unit cell l located in cluster ψ_H with weighting factor w_{Il} and another generic unit cell k; $\left\{ \boldsymbol{f}^{k\alpha - l\beta}, \boldsymbol{f}^{l\beta - k\alpha} \right\}$ represents a pair of interatomic forces acting on the $k\alpha$th atom and the $l\beta$th atom, $\boldsymbol{f}^{k\alpha - l\beta} = -\boldsymbol{f}^{l\beta - k\alpha}$; through the shape function $\Phi_{kl} = \Phi_l(k)$, force $w_H \Phi_{kl} \boldsymbol{f}^{k\alpha - l\beta}$ is distributed to the

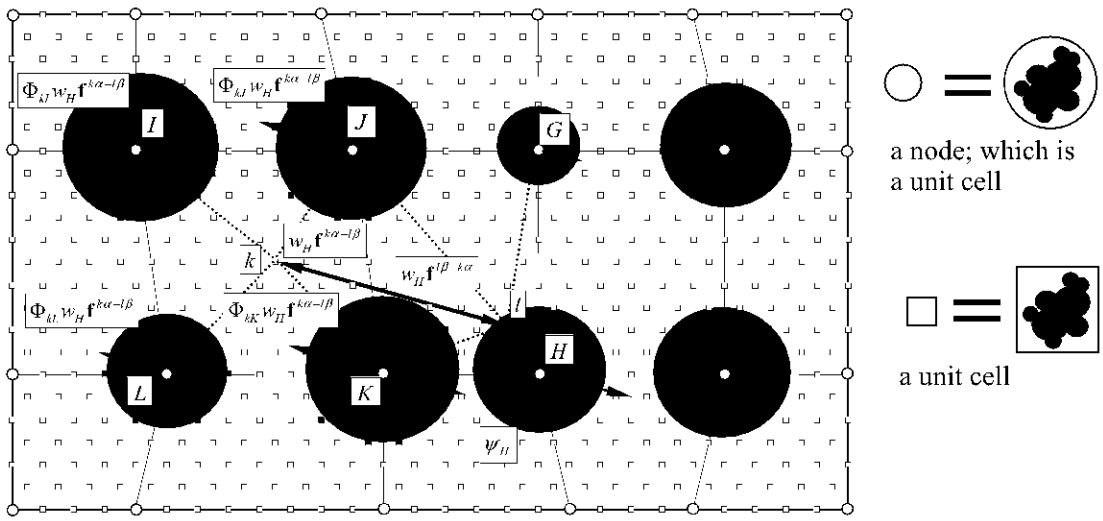

Fig. 4 Schematic of the ABC model with force distributions

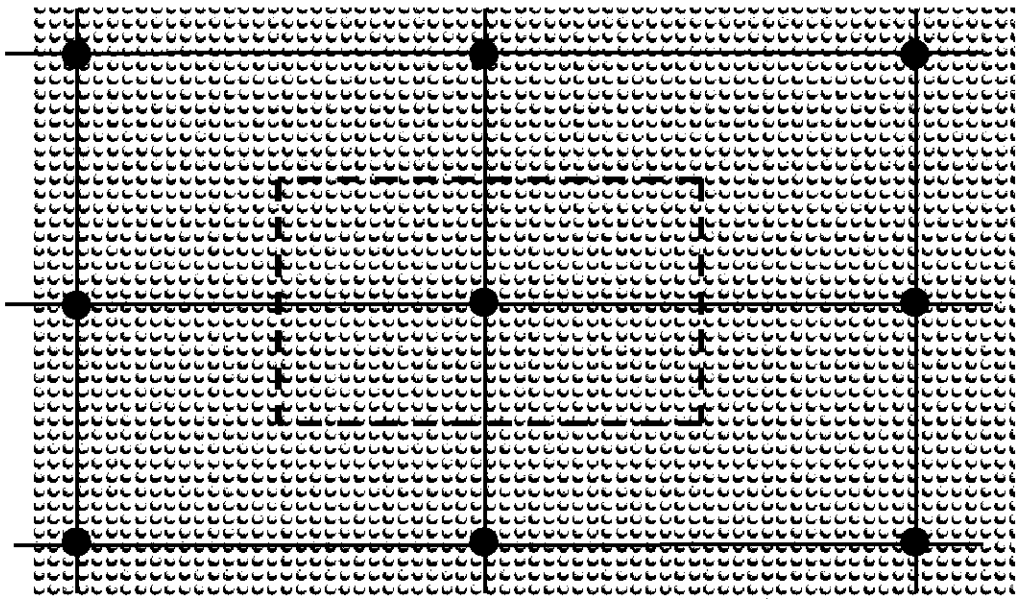

Fig. 5 The coarse-grained FE mesh and the nodal ensemble

αth atom of node I; similarly, $w_H\Phi_{kJ}\boldsymbol{f}^{k\alpha\ J\beta}$, $w_{II}\Phi_{kK}\boldsymbol{f}^{k\alpha-J\beta}$, and $w_{II}\Phi_{kL}\boldsymbol{f}^{k\alpha-J\beta}$ are distributed to the αth atom of nodes J, K, and L; in the same way, $w_{II}\Phi_{lJ}\boldsymbol{f}^{l\beta-k\alpha}$, $w_{II}\Phi_{lK}\boldsymbol{f}^{l\beta-k\alpha}$, $w_{II}\Phi_{lG}\boldsymbol{f}^{l\beta-k\alpha}$, and $w_H\Phi_{lI}\boldsymbol{f}^{l\beta\ k\alpha}$ are distributed to the βth atom of nodes J, K, G and H. Let $\{\boldsymbol{f}^{m\alpha-\eta}, \boldsymbol{f}^{\eta-m\alpha}\}$ represent a pair of interatomic forces acting on the ηth atom in the continuum region and the ηth atom in the atomic region.

4 Coarse-Grained Non-Equilibrium Simulation

Figure 5 is a conceptual illustration of the CG-NES algorithm. In Fig. 5, the grey solid circle represents a unit cell; the black solid circle means a FE node; the area surrounded by the dashed line is called the nodal ensemble with node I, i.e. the Wigner-Seitz region of node I. In the proposed model, it is assumed that each nodal ensemble is viewed as a local thermal reservoir representing the thermal space of a large number of unit cells. Note that the nodal ensemble is defined by the Wigner-Seitz region, which depends on the FE discretization.

The essence of the proposed CG-NES algorithm is: the FE node's motion is determined by the external mechanical and thermal loading; whereas the atom's motion in each finite element is controlled by the corresponding FE nodes through the shape

functions; each FE node's thermal properties such as temperature are calculated by the motion of atoms in each corresponding nodal ensemble. In a comparison between the temperature of the nodal ensemble and the desired temperature, a feedback input to the controllable FE nodes drives the system.

Since at the coarse-scale level the temperature distribution is not uniform and evolved with time, the FE nodal temperature changes from node to node and from time to time. Therefore, to control the temperature of some specified nodes, a distributed Nosé-Hoover thermostat network is necessary to ensure that each nodal ensemble reaches a desired temperature. This is called as a generalized Nosé-Hoover thermostat. The conventional Nosé-Hoover thermostat renders the MD system a canonical ensemble, while this proposed model offers a coarse-grained canonical ensemble, that is a generalized notion of a canonical ensemble in non-equilibrium simulation.

Following the idea of the Nosé-Hoover thermostat, a damping force, with a possible positive and negative damping coefficient, is used as an external force in FE analysis for the coarse-grained non-equilibrium process. Following equation (21), the generalized Nosé-Hoover thermostat is proposed at the coarse level for each FE node as

$$\tilde{M}_I^{\alpha}\ddot{\mathbf{U}}_I^{\alpha}=\mathbf{F}_I^{\alpha}+\mathbf{\Phi}_I^{\alpha}-\chi_I\tilde{M}_I^{\alpha}(\mathbf{V}_I^{\alpha}-\bar{\mathbf{v}}_I+\Delta\mathbf{V}_I^{\alpha}) \tag{24}$$

where $\mathbf{V}_I^{\alpha}=\dot{\mathbf{U}}_I^{\alpha}$ is the velocity of the αth atom at node I; $\Delta\mathbf{V}_I^{\alpha}$ is the auxiliary velocity to make sure that the action of the thermostat itself does not change the linear and angular momenta of the Ith nodal ensemble; the dynamical governing equation of χ_I is given as

$$\frac{\mathrm{d}\chi_I}{\mathrm{d}t}=\frac{1}{Q_I}\left[\sum_{k=1}^{N_I}\sum_{\alpha=1}^{N_a}m^{k\alpha}\left(\boldsymbol{v}^{k\alpha}-\bar{\mathbf{v}}_I\right)^2-3k_BN_IN_aT_{\mathrm{eqb}-I}\right] \tag{25}$$

where Q_I is the effective mass of the Ith node; $\boldsymbol{v}^{k\alpha}=\sum_I\Phi_I(k)\mathbf{V}_I^{\alpha}$ is the velocity of the $k\alpha$th atom in the nodal ensemble $\Re_I$; N_I is the number of unit cells within $\Re_I$; $\bar{\mathbf{v}}_I$ is the mass-weighted average velocity of $\Re_I$; $T_{\mathrm{eqb}-I}$ is the desired temperature of $\Re_I$.

On the one hand, note that in a specified non-equilibrium problem, not all FE nodal temperatures are controlled, so the generalized Nosé-Hoover thermostat is only used at the FE nodes of which the temperature is controllable. On the other hand, if one wants to control the temperature of a group of FE nodes, one can assemble the group of FE nodes as a local thermal reservoir.

Table 1 Short-range interaction parameters for different pairs in MgO

Species	Species	A(eV)	ρ(Å)	C(eV(Å)^6)	D(eV(Å)^{12})
O^{2-}	O^{2-}	9547.96	0.2192	32.0	32.0
Mg^{2+}	O^{2-}	1284.38	0.2997	0.00	0.00
Mg^{2+}	Mg^{2+}	0.00000	0.0000	0.00	0.00

This work investigates the thermal phenomena of single-crystal MgO (magnesium oxide) under different mechanical or thermal conditions through the proposed CG-NES algorithm in the following section. For the ionic MgO crystals, the Coulomb–Buckingham potential listed in Table 1 is adopted to derive the interatomic force. The Coulomb–Buckingham potentials between pairs of two atoms, Mg-Mg, O-O and Mg-O, are expressed as

$$U^{\xi\eta}=\frac{q^{\xi}q^{\eta}}{r^{\xi\eta}}+A^{\xi\eta}\exp\left(-\frac{r^{\xi\eta}}{\rho^{\xi\eta}}\right)-\frac{C^{\xi\eta}}{(r^{\xi\eta})^6} \tag{26}$$

where $A^{\xi\eta}$, $\rho^{\xi\eta}$, and $C^{\xi\eta}$ are material constants; $r^{\xi\eta}\equiv\left\|\boldsymbol{r}^{\xi\eta}\right\|\equiv\left\|\boldsymbol{r}^{\xi}-\boldsymbol{r}^{\eta}\right\|$.

5 NUMERICAL EXAMPLES

5.1 Validation

To validate the proposed CG-NES algorithm, the analysis of a 3D heat conduction problem with finest FE mesh (i.e. the size of the finite element is equal to the lattice constant of the crystal) has been performed as a benchmark example and has been compared with the results from pure MD simulation. From Fig. 6, it is shown that the 3D molecular dynamical model (1.68 nm × 22.26 nm) and the CG-NES model (1350 nodes and 848 finite elements) with finest FE mesh of MgO crystal are subjected to different thermostats at both ends of the specimen. It is seen that the atoms or nodes at both ends of the specimen were fixed; and the heat sink region T_L = 280K and heat source region T_H = 320K are used to simulate a temperature gradient. Here a certain number of nodes are assumed to assemble as a group to calculate the temperature. In other words, the nodes in the same group have the same temperature and use the same friction coefficient for temperature control if they are located in the heat sink or source region. The system is first relaxed for 40 pico seconds (ps) at 300K for equilibrating. The time step Δt is fixed at 1 femto second (fs) for all simulations in this work. Then the Nosé-Hoover thermostat

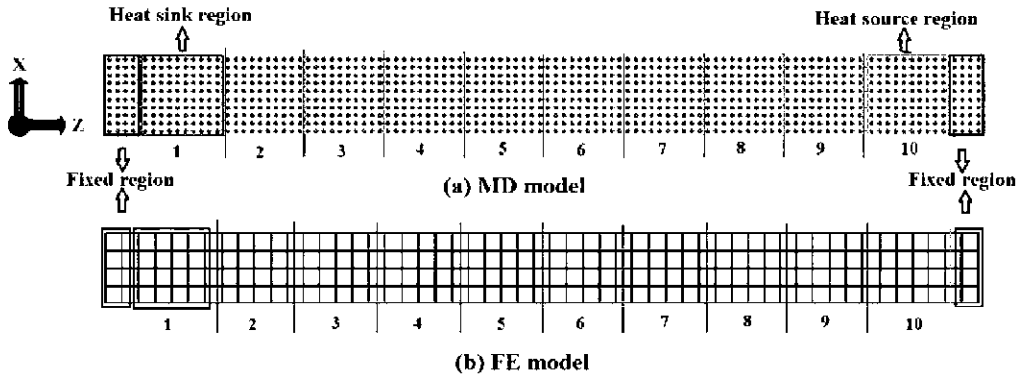

Fig. 6 Three-dimensional heat conduction model: (a) MD model; (b) FE model

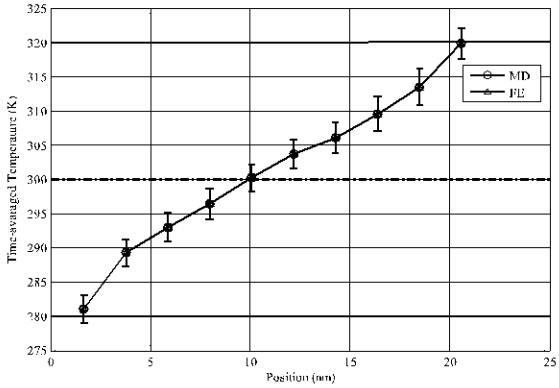

Fig. 7 Comparison of temperature profile between MD simulation and FE simulation

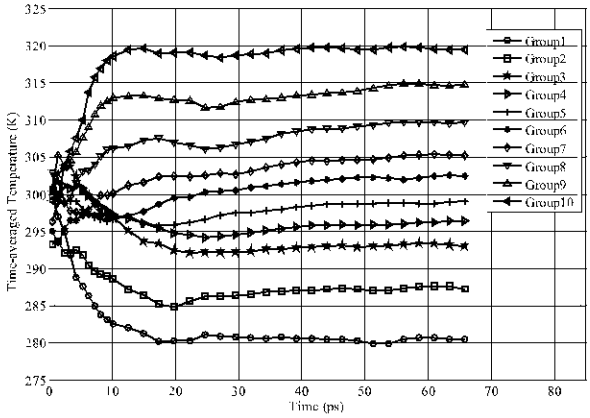

Fig. 8 Temperature evolution with time at different groups

is applied at the heat sink and source regions. From Fig. 7, it is seen that the temperature profile from MD simulation and CG-NES simulation are exactly the same as expected, since CG-NES can be reduced to MD simulation when the size of the finite element is equal to the lattice constant of the crystal. This indicated the reliability and capability of CG-NES for non-equilibrium systems. Here each group's temperature is assumed to be averaged at each pico second. Figure 8 shows the evolution of the time-averaged temperature of each group. It is noticed that it takes time for the temperature of each group to reach the equilibrium state and that the governing equation of temperature acts like a diffusion equation as in the classical heat transfer. However, it is emphasized that this work has never used the Fourier's law to link heat flux with temperature gradient; in fact, the diffusion equation for temperature was not solved because temperature is a dependent variable in MD and in CG-NES as well.

5.2 Effects of reference temperature

In classical heat conduction, Fourier's law stipulates that heat flux depends on the temperature gradient. However, in atomistic simulations, it does not require any *a priori* phenomenological constitutive equation of heat transfer such as Fourier's law. In other words, atomistic simulation indicates that heat flux could be a function of temperature (or reference temperature), strain rate, temperature gradient, etc. Here, the effects of reference temperature (initial temperature right after relaxation) on the temperature distribution are studied for a longer specimen (1.68 nm × 43.26 nm) with 2600 nodes and 1648 finite elements depicted in Fig. 9. In this case the special region in Fig. 9 is a fixed region. Region 1 and region 20 are simulated as heat sink and heat source, respectively. In order to single out the effect of reference temperature on the heat conduction, the temperature gradient was fixed to be 80K. Two cases are simulated: one with reference temperature $T = 260$ K; the other with $T = 300$ K. Comparing Fig. 10(a) with Fig. 10(b), it is observed that the reference temperature has a significant influence on the temperature distribution of the specimen. Also from Fig. 10(b), it is seen that the temperature distribution does not follow the

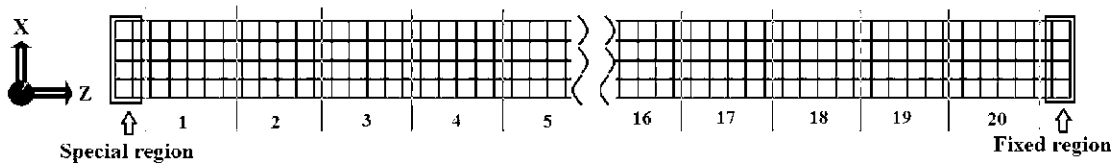

Fig. 9 Three-dimensional heat conduction FE model with 20 groups

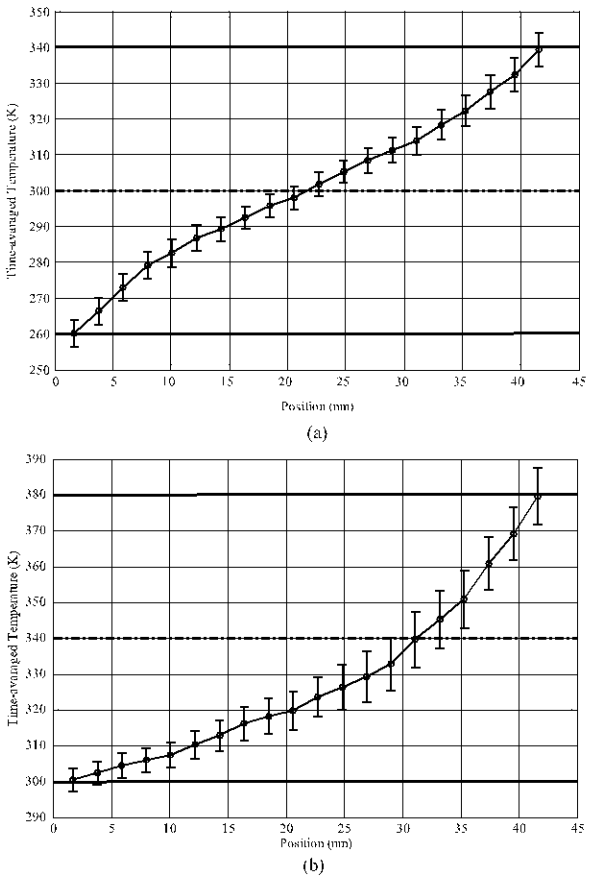

Fig. 10 Temperature profile under different initial equilibrium state: (a) initial state with $T = 260$K; (b) initial state with $T = 300$K

Fourier's law of thermal conduction. This confirms that the Fourier's law of heat conduction is not valid in nanostructures [**37**, **38**]. However, it was found that the temperature distribution is monotonic, although not linear, between the heat sink and the heat source.

5.3 Heat conduction at coarse scale

In this example, consider a coarse-scale FE system shown in Fig. 11. The FE mesh of this specimen (3.36 nm × 3.36 nm × 53.76 nm) has 315 nodes and 136 elements. Two groups of nodes at both ends of the specimen are used to control the temperature and the nodal ensemble is adopted to calculate the temperature of each nodal point. From Fig. 12, it is shown that the temperature distribution is very similar to that in the finest FE model. This once again verifies that the CG-NES algorithm can be utilized to simulate the thermo-mechanical process and to calculate the temperature of a non-equilibrium system. Figure 13 shows that the temperature of different nodes evolves with time, indicating that the variation of temperature satisfies the diffusion equation and it takes time to reach the equilibrium state.

5.4 Shock wave and electromagnetic wave

In order to show the advantage of CG-NES in thermo-mechanical coupling and to present the capability of CG-NES to account for thermal-electromagnetic effects, a 3D mechanical wave propagation along the z-direction of the specimen and a 3D problem subject to a given electromagnetic field are simulated. The FE model is shown in Fig. 9.

In the case of mechanical wave propagation, the system is assumed to be initially at rest after a period of relaxation time and the boundary conditions are set as

$$u_z^{\alpha}(x, y, 43.26\,\text{nm}, t) = 0 \tag{28}$$

$$u_z^{\alpha}(x, y, 0, t) = \begin{cases} 0.21 \sin(\pi t/2) & \text{if } t \leqslant 2\text{ps} \\ 0 & \text{if } t \geq 2\text{ps} \end{cases} \tag{29}$$

The purpose of a long period of relaxation before simulation is to rule out other noise effects owing to reference temperature and to make the correlations between wave propagation and temperature variation more pronounced.

Figure 14 shows the displacement and the corresponding temperature of two different groups at $z = 12.18$ nm and at $z = 28.98$ nm. It is clearly seen from Fig. 14(a) and Fig. 14(c) that the shock wave

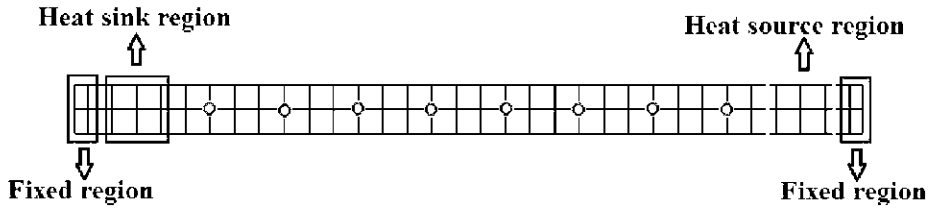

Fig. 11 Coarse-scale FE model with heat sink and source region

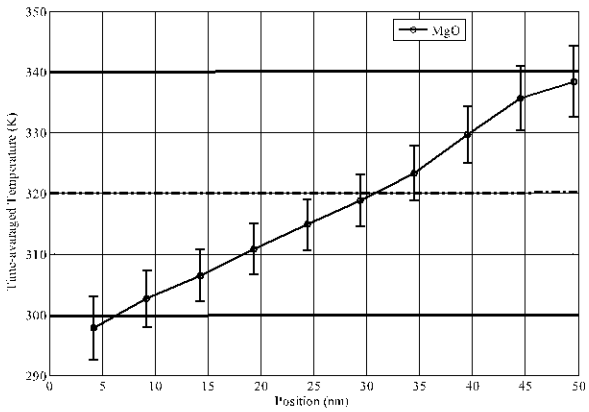

Fig. 12 Temperature profile at coarse scale

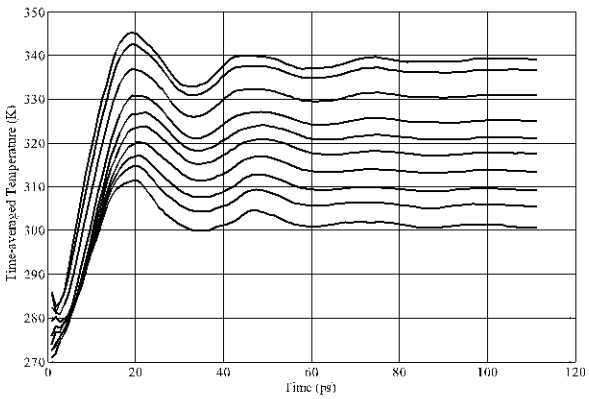

Fig. 13 Temperature evolution with time

propagates along the z-direction and reflects at the boundary (z = 43.26 nm). One may find that, as the time goes on, the maximum amplitude of the displacement decreases. This is attributed to the fact that, once the energy associated with the wave is converted into heat, it tends to spread out over the entire domain rather than convert back again. It is also observed that there is a correlation between the movements of the high temperature peak and the wave front. The simulation results predict that the interchange of different forms of energies will generate non-uniform temperature distribution, indicating the capability of the CG-NES method to simulate non-equilibrium processes.

In the case of the electromagnetic wave, for each node the initial displacement is obtained and initial velocity is reduced to zero after a long time of relaxation. No loading and no boundary constraints are applied in the simulation. The body forces, i.e. the Lorentz forces acting on the charged atoms, are caused solely by the external EM field. Here, the harmonic electric field $\mathbf{E}=[E_x\ E_y\ E_z]=[E_x\ 0\ 0]$ and the magnetic flux density $\mathbf{B}=[B_x\ B_y\ B_z]=[0\ B_y\ 0]$ with variance in time and space are given as

$$E_x=B_y=\begin{cases} 0 & \text{if } t<2\pi\omega \\ A\exp[i\omega(z-ct)/c] & \text{if } 2\pi\omega<t<4\pi\omega \\ 0 & \text{if } t>4\pi\omega \end{cases} \quad (29)$$

where c is the speed light, A = 100 μV/nm is the amplitude, and ω = 26THz is the frequency of the EM wave. It is noticed that the electric field and the magnetic flux density specified in equation (29) satisfy Maxwell's equations in vacuum. Here only the effect of EM wave on temperature is studied, not the thermo-mechanical–electromagnetic coupling. Figure 15 shows the temperature evolution of the whole specimen with time. It is seen that the temperature shows a significant increase during the period with the given EM wave, and holds a steady-state value after the EM wave stops. This is attributed to the fact that the work done by the EM wave, through the Lorentz force, converts into both potential energy and kinetic energy; the latter reflects itself in temperature. This indicates that the CG-NES has the ability to investigate the EM effect on the temperature.

6 SUMMARY

In this work, a coarse-grained non-equilibrium method has been formulated, implemented, and tested in numerical computations. The nodal ensemble surrounding each FE node is utilized to compute the temperature field. It has been demonstrated that this proposed model is reliable and

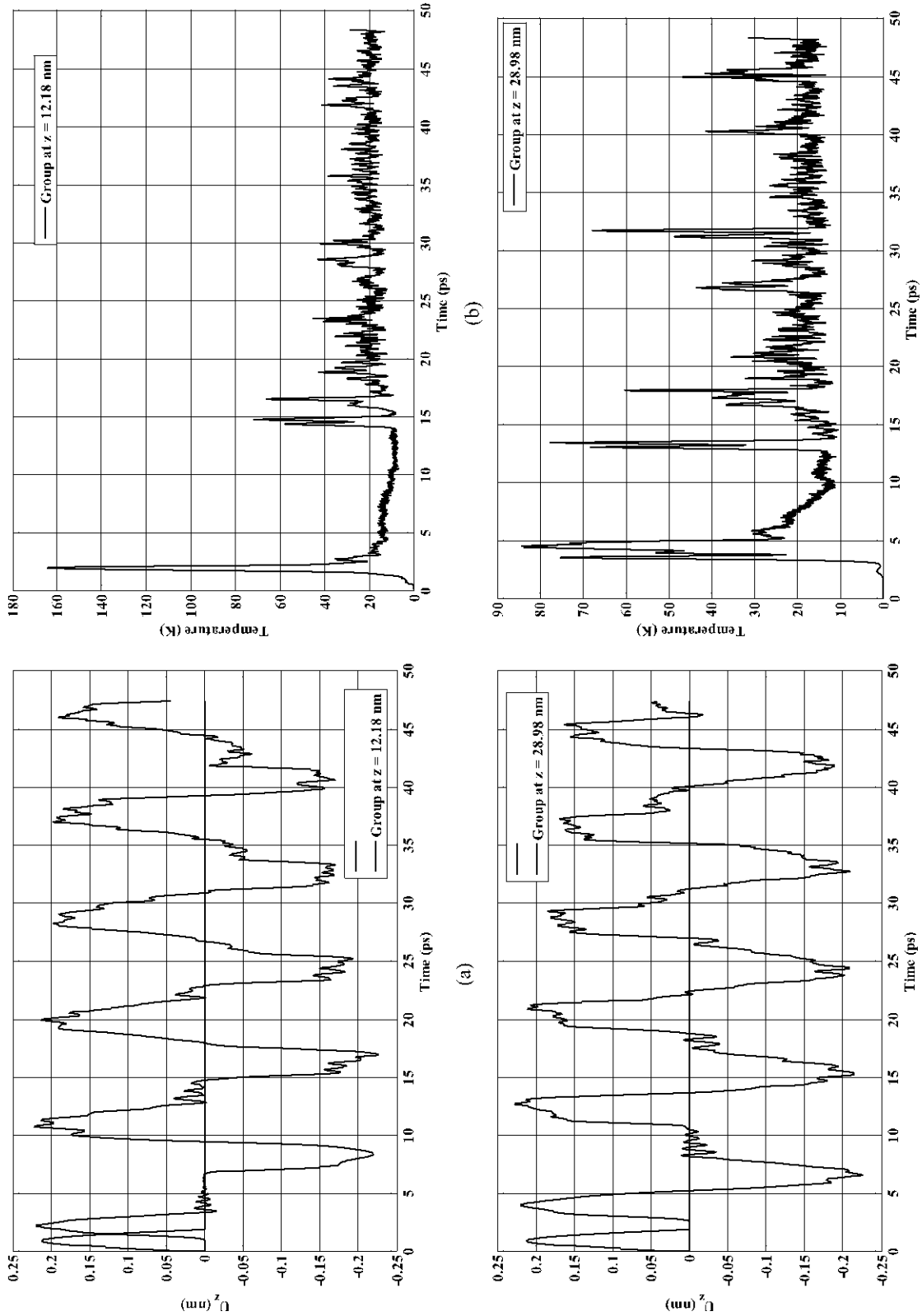

Fig. 14 Displacement profiles and the corresponding temperature profiles under the shock wave: (a) displacement profile at z =12.18 nm; (b) temperature profile at z = 12.18 nm; (c) displacement profile at z = 28.98 nm; (d) temperature profile at z = 28.98 nm

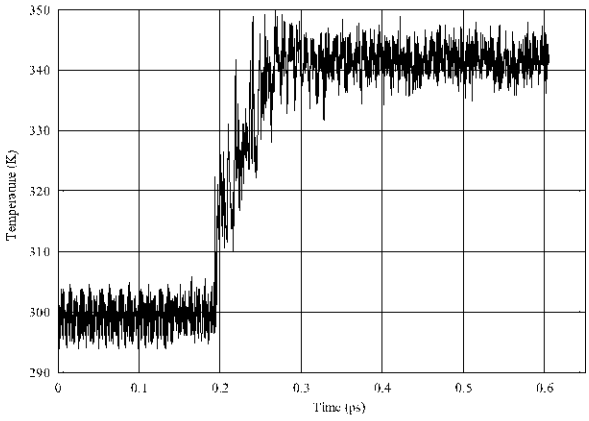

Fig. 15 Temperature evolution with time under electromagnetic wave

efficient, thereby offering a new perspective view for calculating thermal properties at nanoscale. The major findings can be summarized as follows:

(a) The CG-NES method can be naturally reduced to NEMD simulation when the size of the FE mesh is equal to the lattice constant of the crystal;
(b) the reference temperature of the system that is to be simulated has a significant influence on the temperature distribution of the specimen;
(c) the problem of shock wave propagation indicates the ability of CG-NES to simulate the thermo-mechanical coupling process.

REFERENCES

1 **Cahill, D. G., Goodson, K.,** and **Majumdar, A.** Thermometry and thermal transport in micro/nanoscale solid-state devices and structures. *J. Heat Transfer, Trans. ASME*, 2002, **124**, 223–241.
2 **Chen, G.** and **Shakouri, A.** Heat transfer in nanostructures for solid-state energy conversion. *J. Heat Transfer, Trans. ASME*, 2002, **124**, 242–252.
3 **Kulish, V. V., Lage, J. L., Komarov, P. L.,** and **Raad, P. E.** A fractional-diffusion theory for calculating thermal properties of thin films from surface transient thermoreflectance measurements. *J. Heat Transfer, Trans. ASME*, 2001, **123**, 1133–1138.
4 **Wang, X. W., Hu, H. P.,** and **Xu, X. F.** Photo-acoustic measurement of thermal conductivity of thin films and bulk materials. *J. Heat Transfer, Trans. ASME*, 2001, **123**, 138–144.
5 **Zhang, F., Isbister, D. J.,** and **Evans, D. J.** Nonequilibrium molecular dynamics simulations of heat flow in one-dimensional lattices. *Phys. Rev. E*, 2000, **61**, 3541.
6 **Evans, D. J.** Homogeneous NEMD algorithm for thermal conductivity. Application of non-canonical linear response theory. *Phys. Lett. A*, 1982, **91**, 457–460.
7 **Zhang, M. M., Lussetti, E., de Souza, L. E. S.,** and **Muller-Plathe, F.** Thermal conductivities of molecular liquids by reverse nonequilibrium molecular dynamics. *J. Phys. Chem. B*, 2005, **109**, 15060–15067.
8 **Hoover, W. G., Evans, D. J., Hickman, R. B., Ladd, A. J. C., Ashurst, W. T.,** and **Moran, B.** Lennard-Jones triple-point bulk and shear viscosities. Green-Kubo theory, Hamiltonian mechanics, and nonequilibrium molecular dynamics. *Phys. Rev. A*, 1980, **22**, 1690.
9 **Evans, D. J.** and **Morriss, G. P.** Nonlinear-response theory for steady planar couette-flow. *Phys. Rev. A*, 1984, **30**, 1528–1530.
10 **Edwards, B. J., Baig, C.,** and **Keffer, D. J.** An examination of the validity of nonequilibrium molecular-dynamics simulation algorithms for arbitrary steady-state flows. *J. Chem. Phys.*, 2005, **123**, 114106.
11 **Hoover, W. G., Ladd, A. J. C.,** and **Moran, B.** High-strain-rate plastic flow studied via nonequilibrium molecular dynamics. *Phys. Rev. Lett.*, 1982, **48**, 1818.
12 **Holian, B. L.** and **Lomdahl, P. S.** Plasticity induced by shock waves in nonequilibrium molecular-dynamics simulations. *Science*, 1998, **280**, 2085–2088.
13 **Kroumlger, M.** and **Makhloufi, R.** Wormlike micelles under shear flow: A microscopic model studied by nonequilibrium-molecular-dynamics computer simulations. *Phys. Rev. E*, 1996, **53**, 2531.
14 **Kroumlger, M.** and **Hess, S.** Rheological evidence for a dynamical crossover in polymer melts via nonequilibrium molecular dynamics. *Phys. Rev. Lett.*, 2000, **85**, 1128.
15 **Xu, L., Sedigh, M. G., Sahimi, M.,** and **Tsotsis, T. T.** Nonequilibrium molecular dynamics simulation of transport of gas mixtures in nanopores. *Phys. Rev. Lett.*, 1998, **80**, 3511.
16 **Abraham, F. F., Broughton, J. Q., Bernstein, N.,** and **Kaxiras, E.** Spanning the continuum to quantum length scales in a dynamic simulation of brittle fracture. *Europhys. Lett.*, 1998, **44**, 783–787.
17 **Rudd, R. E.** and **Broughton, J. Q.** Coarse-grained molecular dynamics and the atomic limit of finite elements. *Phys. Rev. B*, 1998, **58**, R5893–R5896.
18 **Park, H. S., Karpov, E. G., Liu, W. K.,** and **Klein, P. A.** The bridging scale for two-dimensional atomistic/continuum coupling. *Philosoph. Mag.*, 2005, **85**, 79–113.
19 **Wagner, G. J.** and **Liu, W. K.** Coupling of atomistic and continuum simulations using a bridging scale decomposition. *J. Comput. Phys.*, 2003, **190**, 249–274.
20 **Bozzolo, G., Noebe, R. D.,** and **Abel, P. B.** *Applied computational materials modeling: theory, simulation, and experiment*, 2007 (Springer, New York, NY).

21 **E, W. N., Engquist, B., Li, X. T., Ren, W. Q.,** and **Vanden-Eijnden, E.** Heterogeneous multiscale methods: a review. *Commun. Comput. Phys.*, 2007, **2**, 367–450.

22 **E, W. N.** and **Huang, Z. Y.** Matching conditions in atomistic-continuum modeling of materials. *Phys. Rev. Lett.*, 2001, **87**, 135501.

23 **Li, S. F.** and **Sheng, N.** On multiscale non-equilibrium molecular dynamics simulations. *Int. J. Numer. Methods Engng*, 2010, **83**, 998–1038.

24 **Li, S. F., Sheng, N.,** and **Liu, X. H.** A non-equilibrium multiscale simulation paradigm. *Chem. Phys. Lett.*, 2008, **451**, 293–300.

25 **Sheng, N.** and **Li, S. F.** A non-equilibrium multi-scale simulation of shock wave propagation. *Mech. Res. Commun.*, 2008, **35**, 10–16.

26 **Baranyai, A.** Heat flow studies for large temperature gradients by molecular dynamics simulation. *Phys. Rev. E*, 1996, **54**, 6911.

27 **Muller-Plathe, F.** A simple nonequilibrium molecular dynamics method for calculating the thermal conductivity. *J. Chem. Phys.*, 1997, **106**, 6082–6086.

28 **Lepri, S., Livi, R.,** and **Politi, A.** Thermal conduction in classical low-dimensional lattices. *Phys. Reports*, 2003, **377**, 1–80.

29 **Poulikakos, D., Arcidiacono, S.,** and **Maruyama, S.** Molecular dynamics simulation in nanoscale heat transfer: A review. *Microscale Thermophys. Engng*, 2003, **7**, 181–206.

30 **Castejon, H. J.** Nonequilibrium molecular dynamics calculation of the thermal conductivity of solid materials. *J. Phys. Chem. B*, 2002, **107**, 826–828.

31 **Tokumasu, T.** and **Kamijo, K.** Molecular dynamics study for the thermal conductivity of diatomic liquid. *Superlattices and Microstructures*, 2004, **35**, 217–225.

32 **Chantrenne, P.** and **Barrat, J.** Finite size effects in determination of thermal conductivities: comparing molecular dynamics with simple models. *ASME J. Heat Transfer*, 2004, **126**, 577–585.

33 **Hoover, W. G.** Canonical dynamics – equilibrium phase-space distributions. *Phys. Rev. A*, 1985, **31**, 1695–1697.

34 **Hoover, W. G.** and **Hoover, C. G.** Nonequilibrium molecular dynamics. *Condensed Matter Phys.*, 2005, **8**, 247–260.

35 **Martyna, G., Klein, M.,** and **Tuckerman, M.** Nosé-Hoover chains: the canonical ensemble via continuous dynamics. *J. Chem. Phys.*, 1992, **97**, 2635–2645.

36 **Berendsen, H. J. C., Postma, J. P. M., Vangunsteren, W. F., Dinola, A.,** and **Haak, J. R.** Molecular-dynamics with coupling to an external bath. *J. Chem. Phys.*, 1984, **81**, 3684–3690.

37 **Chang, C. W., Okawa, D., Garcia, H., Majumdar, A.,** and **Zettl, A.**, 2008, Breakdown of Fourier's law in nanotube thermal conductors. *Phys. Rev. Lett.*, 2008, **101**, 075903.

38 **Yang, N., Zhang, G.,** and **Li, B.** Violation of Fourier's law and anomalous heat diffusion in silicon nanowires. *Nano Today*, 2010, **5**, 85–90.

APPENDIX

Suppose we have a group of atoms N, not a whole specimen. We want to use the Nosé-Hoover thermostat to control the temperature. The key point is that the linear and angular momenta associated with the Nosé-Hoover thermostat should be zero. Notice that now the linear and angular momenta are not zero.

Linear momentum

$$\mathbf{P}=\sum_{i=1}^{N} m^i \boldsymbol{v}^i \neq 0 \tag{1}$$

Angular momentum

$$\mathbf{H}=\sum_{i=1}^{N} m^i \boldsymbol{r}^i \times \boldsymbol{v}^i \neq 0 \tag{2}$$

Here it is emphasized that the origin is the centroid of this group of atoms, i.e.

$$\sum_{i=1}^{N} m^i \boldsymbol{r}^i = 0 \tag{3}$$

Define

$$M \equiv \sum_{i=1}^{N} m^i \tag{4}$$

$$r \equiv \|r\|, \qquad H \equiv \|\mathbf{H}\| \tag{5}$$

$$I \equiv \sum_{i=1}^{N} m^i \boldsymbol{r}^i \cdot \boldsymbol{r}^i \tag{6}$$

Now the velocity of every atom is changed to $\boldsymbol{v}^i + \Delta \boldsymbol{v}^i$ where

$$\Delta \boldsymbol{v}^i \equiv \boldsymbol{r}^i \times \mathbf{H}/I - \mathbf{P}/M \tag{7}$$

It is straightforward to demonstrate that

$$\begin{aligned}
\mathbf{H}^* &= \sum_{i=1}^{N} m^i \mathbf{r}^i \times (\mathbf{v}^i + \Delta \mathbf{v}^i) = \mathbf{H} + \sum_{i=1}^{N} m^i \mathbf{r}^i \times \Delta \mathbf{v}^i \\
&= \mathbf{H} + \sum_{i=1}^{N} m^i \mathbf{r}^i \times \{(\mathbf{r}^i \times \mathbf{H})/I - \mathbf{P}/M\} \\
&= \mathbf{H} + \sum_{i=1}^{N} m^i \mathbf{r}^i \times (\mathbf{r}^i \times \mathbf{H})/I + \mathbf{P} \times \{\sum_{i=1}^{N} m^i \mathbf{r}^i\}/M \\
&= \sum_{i=1}^{N} m^i (\mathbf{r}^i \cdot \mathbf{H}) \mathbf{r}^i / I \\
&\neq 0
\end{aligned} \tag{8}$$

$$\begin{aligned}\mathbf{P}^* &= \sum_{i=1}^{N} m^i(\boldsymbol{v}^i+\Delta\boldsymbol{v}^i)=\mathbf{P}+\sum_{i=1}^{N} m^i\Delta\boldsymbol{v}^i \\ &=\mathbf{P}+\sum_{i=1}^{N} m^i\{(r^i\times\mathbf{H})/I-\mathbf{P}/M\} \\ &=\sum_{i=1}^{N} m^i\boldsymbol{r}^i\times\mathbf{H}/I \\ &=0\end{aligned} \tag{9}$$

Now we make a test. If $\|\mathbf{H}^*\|/\|\mathbf{H}\|$ is less than a specified tolerance, we may consider that the linear and angular momenta of the group are almost unchanged during the whole process. If not, we update the velocity of every atom according to Eq. (7) through $\mathbf{H}^*$ and $\mathbf{P}^*$, calculate the new $\mathbf{H}^*$ and $\mathbf{P}^*$ according to Eqs. (8) and (9) until the test is satisfied.